Journal of Energy Chemistry 72 (2022) 509–515

Contents lists available at ScienceDirect

Journal of Energy Chemistry

journal homepage: www.elsevier.com/locate/jechem

http://www.journals.elsevier.com/journal-of-energy-chemistry/

The surface of metal boride tinted by oxygen evolution reaction for enhanced water electrolysis

Xu Zou, Wei Zhang *, Xinyan Zhou, Kexin Song, Xin Ge, Weitao Zheng *

Key Laboratory of Automobile Materials MOE, School of Materials Science & Engineering, and Jilin Provincial International Cooperation Key Laboratory of High-Efficiency Clean Energy Materials, Electron Microscopy Center, and International Center of Future Science, Jilin University, Changchun 130012, Jilin, China

ARTICLE INFO

Article history:
Received 30 April 2022
Revised 25 May 2022
Accepted 27 May 2022
Available online 6 June 2022

Keywords:
Inverted design
Self-functional surfaces
Metal borate
Water splitting
Oxygen evolution reaction

ABSTRACT

Oxygen evolution reaction (OER) is a bottleneck half-reaction in many important energy conversion processes (*e.g.*, water splitting), and one of the key issues lies to develop high-efficiency, cost-effective OER electrocatalysts. Rather than those popular extrinsic modulations of any catalysts with gradually degraded performance, we aim at the utilization of the intermediates offered from the undergoing OER as long-standing electrocatalysts. Herein, by inverted design, we extracted the bimetallic borides ($FeCoB_2$)-derived intermediates metal borates in the OER, unlocking their potential as a self-functionalized highly active catalytic phase *in-situ* formed on the metal boride surface for continuing OER operation. Mechanistically, the surface metal atoms are oxidized to oxyhydroxides, and the surface metalloids (B) are further transformed to the corresponding oxoanions to form metal borates. Such OER self-produced electrocatalyst exhibits a small overpotential of 295 mV at 10 mA/cm^2 and its high catalytic activity lasts even after 200 h. Compared with $FeCoB_2$, the catalytic activity of this electrochemically activated $FeCoB_2$ is ~7 times higher. The *in-situ* formed metal borate is dominatingly responsible for the obtained high catalytic activity. Such unique OER-produced self-functionalization surfaces of metal borates afford to greatly reduce the energy barrier of the continuing OER, thereby accelerating the reaction process.

1. Introduction

Water electrolysis ($2H_2O \rightarrow 2H_2 + O_2$) powered by renewable energy (*e.g.*, solar and wind) provides a sustainable strategy for large-scale production of hydrogen (H_2) and recovery of chemical energy from H_2 [1–6]. Although its technical feasibility has been demonstrated, an efficient process has not been realized, which is mainly limited by the sluggish oxygen evolution reaction (OER). In addition, the working environment of catalytic materials during the OER is very harsh (*e.g.*, strong acid/base and strong oxidizing properties), which leads to the susceptibility of the material surface to phase changes and atomic leaching [7,8]. Such scenarios reduce the activity and stability of the electrocatalysts [9–12]. Breakthroughs will require the development of cost-effective and efficient electrocatalysts [13,14]. In recent years, much effort has been made to find transition metal-based (*e.g.*, Mo, W, Co, Ni, and Fe) OER catalysts [15–19]. Among them, iron has a significant advantage. On the one hand, iron is the abundant metal in the Earth's crust, which is much cheaper than other metal electrocatalysts. On the other hand, iron-based catalysts can serve as mediators for some biological processes in nature [20,21]. In inverted design, rather than dealing with popular architectures of targeting electrocatalysts, we aim to unlock the full potential of a multicomponent material in circumstance of OER, with any possibility to produce a reaction self-produced phase state for any continuing and higher-efficiency OER, which is of great interests and challenging.

Transition metal borides (TMBs) are a class of metalloid boron-containing alloy compounds with well-defined stoichiometry and organized crystal structures [22]. More importantly, TMBs exhibit ionic, covalent, and metallic bonding behaviors, which endow them with many unique physicochemical properties, such as superconducting, high hardness and permanent magnetism [22–25]. Recent studies have shown that single and mixed transition metal borides are potentially effective electrocatalysts for water splitting [26,27]. Moderately electronegative boron ($\chi_{Pauling}$ = 2.04) can reduce the energy barrier of metal oxidation reaction and facilitate charge transfer, so that metal borides/borates exhibit better OER performance [26–30]. However, there remains a general lack of knowledge upon unraveling the catalytically active phase of

* Corresponding authors.
E-mail addresses: weizhang@jlu.edu.cn (W. Zhang), wtzheng@jlu.edu.cn (W. Zheng).

https://doi.org/10.1016/j.jechem.2022.05.039

metal boride-derived catalysts. It is usually believed that the catalytically active phase is oxyhydroxide, while others hold a similarity to the NiB_i films [26–30]. Obviously, the precise role of guest elements (B) in enhancing the catalytic performance of host transition metals has not been elucidated. So, it is an open question to in-depth understanding the unique properties of these compounds towards ultimately optimizing the performance of electrocatalysts.

Recently, structural transitions during OER processes have received increasing attention, such as surface oxidation and surface amorphization [27–30]. By a borothermal reduction method, we synthesized bimetallic borides ($FeCoB_2$) assisted by molten salts and captured the $FeCoB_2$-driven intermediates in the OER. We monitor that by unlocking the potential, such *in-situ* self-produced surface state enables a higher-active OER. Such *in-situ* formation of self-functional metal borate containing the oxyhydroxide has a thickness of 5–15 nm on the $FeCoB_2$ surface. Theoretical calculation results show that the transformation of the non-metallic guest greatly improves the OER activity of the electrocatalyst. This *in-situ* formed film exhibits excellent OER activity and stability under alkaline conditions (1 M KOH), requiring only an overpotential of 295 mV to reach a current density of 10 mA/cm^2. In particular, the Tafel slope of this delicate material is ~84 mV/dec and its excellent catalytic activity remained even after 200 h of the continuous OER operation. The OER activity of this electrochemically activated catalytic material is ~7 times higher than that of $FeCoB_2$. Our work motivates us to design a variety of metal borides as precursors and *in-situ* build self-produced functional surfaces to enhance the activity of catalysts. Thus, it may provide a new strategy for designing high-performance electrocatalytic materials for a wide range of electrocatalytic reactions, *e.g.*, OER.

2. Experimental

2.1. Experimental section

2.1.1. Chemicals and reagents

Potassium chloride (KCl), boron (B), ferric sesquioxide (Fe_2O_3), boric acid (H_3BO_3) and Nafion® perfluorinated resin solution were purchased from Aladdin Chemistry Co., Ltd. Cobalt oxide (Co_2O_3), sodium chloride (NaCl), potassium hydroxide (KOH), iron chloride hexahydrate ($FeCl_3{\cdot}6H_2O$) and cobalt chloride hexahydrate ($CoCl_2{\cdot}6H_2O$) were purchased from Sinopharm Chemical Reagent Co., Ltd. RuO_2 was purchased from Sigma-Aldrich. Highly purified water (>18 MΩ cm resistivity) was obtained from a PALL PURELAB Plus system.

2.1.2. Synthesis of metal boride

The synthesis of $FeCoB_2$ was carried out using molten salt-assisted borothermal reduction. Fe_2O_3 (0.015 g), Co_2O_3 (0.0375 g), B (0.033 g), KCl (1.5 g) and NaCl (1.168 g) were fully ground and put into crucible. The crucible was placed in a tube furnace and heated at 1000 °C for 1 h at a heating rate of 10 °C/min. This process is carried out under Ar gas conditions. After cooling to room temperature, the calcined samples were washed 3 times with warm water at 80 °C to remove inorganic salts and by-products (B_yO_z). Final samples were washed with ethanol and dried in a vacuum oven.

The synthesis process of FeB and CoB is similar to that of $FeCoB_2$. The difference between them is that the corresponding metal oxide (Fe_2O_3, Co_2O_3) is not added during the synthesis.

2.1.3. Synthesis of $FeCoBO_4$

$FeCl_3{\cdot}6H_2O$ (0.404 g), $CoCl_2{\cdot}6H_2O$ (0.291 g) and H_3BO_3 (0.47 g) were fully ground and put into a crucible. The crucible was placed in a tube furnace and heated at 300 °C for 2 h and 1000 °C for 8 h at a heating rate of 3 °C/min. This process is carried out under air conditions. After cooling to room temperature, the calcined samples were washed 3 times with deionized water. Final samples were washed with ethanol and dried in a vacuum oven.

2.1.4. Characterizations

Powder X-ray diffraction (PXRD) of metal borides was recorded on a Rigaku D/Max 2550 X-ray diffractometer. The diffraction angle ranged from 10-80° and the scanning speed was 7°/min. The scanning electron microscopy (SEM) images were obtained with a HITACHI, SU8010 electron microscope. Transmission electron microscopy (TEM) images were obtained with a JEOL, JEM-2100F. Electron energy loss spectroscopy (EELS) was recorded using a JEM ARM 300F GRAND ARM. The X-ray photoelectron spectroscopy (XPS) was performed on a Thermo Scientific K-Alpha + X-ray photoelectron spectrometer. Soft X-ray emission spectrometer (SXES) was operated using X-ray spectrometer SS-94000SXES mounted on JSM-7900F [31]. The X-ray absorption spectra (XAS) of Co K-edge and Fe K-edge were collected at 4B9A diffraction experimental station in Beijing Synchrotron Radiation Facility (BSFR). XANES data were normalized by the Athena module of Demeter software packages. EXAFS data were obtained by Fourier transform.

2.1.5. Electrochemical measurements

The electrochemical performance was investigated in a three-electrode system using a CH Instrument (Model 660E). The Hg/HgO electrode was used as the reference electrode in an alkaline (1.0 M KOH solution) system, and the carbon rod was used as the counter electrode. Metal borides are used as working electrodes. The preparation method is as follows: (1) the 4 mg sample was uniformly dispersed into 200 μL of isopropanol and 200 μL of conductive polymer binder (0.3% Nafion solution); (2) drop 2 μL on a glassy carbon electrode (GCE) with a diameter of 3 mm and let it dry; (3) 2 μL of conductive polymer binder was dropped on it and used as a working electrode after drying. The loading is 0.281 mg cm^{-2}. N_2 was continuously pumped into the electrochemical cell during the test. Linear sweep voltammetry (LSV) measurements were made at a scan rate of 0.5 mV/s and 85% *iR*-correction. Chronopotentiometry was used to evaluate the stability of the material at a current density of 10 mA/cm^2 and without *iR*-correction. The potential was converted to the potential *versus* reversible hydrogen electrode (RHE) under alkaline conditions according to the following formula.

$$E_{\text{vs RHE}} = E_{\text{vs Hg/HgO}} + E^{\circ}_{\text{Hg/HgO}} + 0.059\text{pH} \quad (1)$$

Calibration of the reference electrode was performed according to the method reported by Boetter and co-workers [32]. For comparison, the catalytic activity of RuO_2 was evaluated under the same experimental conditions and loadings.

The j_{ECSA} (mA/cm^2) was normalized by the electrochemical active surface area (ECSA) according to the formula.

$$j_{\text{ECSA}} = \frac{i \times 100}{\text{ECSA}} \quad (2)$$

where i is the current obtained after 85% *iR*-correction and ECSA is the corresponding electrochemical surface area of the catalyst.

The ECSA of the catalysts was estimated from the value of its electrochemical double layer capacitance (C_{dl}), as reported by Jaramillo and co-workers [33]. C_{dl} can be obtained by cyclic voltammetry (CV) at various scan rates (20, 40, 60, 80, 100, 110, 120, 130, 140 mV/s) in the voltage range of −0.106 and −0.206 V *vs.* SCE. A linear trend was observed by plotting the difference in anodic and cathodic currents (i_{anodic}-$i_{cathode}$) at −0.156 V *vs* SCE versus scan rate. C_{dl} is half the slope of the fitted line. Calculate the ECSA value of the catalyst according to the formula.

$$\mathrm{ECSA} = \frac{C_{\mathrm{dl}}}{C_{\mathrm{s}}} \tag{3}$$

where C_s is the specific capacitance of the sample, which according to literature is 0.04 mF/cm^2 [33].

Electrochemical impedance spectroscopy (EIS) measurements of the material were performed at a voltage of 0.606 V *vs.* SCE, and a scanning frequency ranging from 100 kHz to 1 Hz.

2.2. Theoretical section

2.2.1. Computation details

All DFT calculations were performed using the Vienna Ab initio Simulation Package (VASP) [34]. The projector augmented wave (PAW) pseudopotential with the PBE generalized gradient approximation (GGA) exchange correlation function was utilized in the computations [35,36]. All energetics of metal oxides were calculated using the DFT with the Hubbard-U framework (DFT + U) to account for strongly localized d-electrons for Fe, Ni. The Hubbard-U correction terms were at U_{eff}(Co) = 3.32 eV and U_{eff}(-Fe) = 5.3 eV as obtained via linear response theory. The cutoff energy of the plane waves basis set was 500 eV and a Monkhorst-Pack mesh of 1 × 1 × 1 was used in K-sampling. All structures were spin polarized and all atoms were fully relaxed with the energy convergence tolerance of 10^{-5} eV per atom, and the final force on each atom was <0.05 eV/Å. Porbaix diagrams were calculated using Atomic Simulation Environment (ASE) with input formation energy by DFT calculations of bulk models [37].

The adsorption energy of reaction intermediates, can be computed using the following Eq. (4).

$$\Delta G_{\mathrm{ads}} = E_{\mathrm{ads}} - E_{*} + \Delta E_{\mathrm{ZPE}} - T\Delta S \tag{4}$$

Where ads = (OH*, O*, OOH*), and (E_{ads}-E_*) is the binding energy, ΔE_{ZPE} is the zero-point energy change, ΔS is the entropy change. In this work, the values of ΔE_{ZPE} and ΔS were obtained by vibration frequency calculation.

The Gibbs free energy of the five reaction steps can be calculated by the following four Eqs. (5)–(8):

$$\mathrm{OH^-} + {}^{*} \leftrightarrow \mathrm{HO^{*}} + \tag{5}$$

$$\Delta G_1 = \Delta G_{\mathrm{HO^*}} - \Delta G_{*} - G_{\mathrm{OH}} - \mathrm{eU}$$

$$\mathrm{HO^{*}} + \mathrm{OH^-} \leftrightarrow \mathrm{O^{*}} + \mathrm{H_2O(l)} + \mathrm{e^-} \tag{6}$$

$$\Delta G_2 = \Delta G_{\mathrm{O^*}} - \Delta G_{\mathrm{HO^*}} - G_{\mathrm{OH}} + G_{\mathrm{H_2O}} - \mathrm{eU}$$

$$\mathrm{O^{*}} + \mathrm{OH^-} \leftrightarrow \mathrm{OOH^{*}} + \mathrm{e^-} \tag{7}$$

$$\Delta G_3 = \Delta G_{\mathrm{OOH^*}} - \Delta G_{\mathrm{O^*}} - G_{\mathrm{OH}} - \mathrm{eU}$$

$$\mathrm{OOH^{*}} + \mathrm{OH^-} \leftrightarrow {}^{*} + \mathrm{O_2} + \mathrm{H_2O(l)} + \mathrm{e^-} \tag{8}$$

$$\Delta G_4 = \Delta G_{*} - \Delta G_{\mathrm{OOH^*}} - G_{\mathrm{OH}} + G_{\mathrm{H_2O}} + G_{\mathrm{O_2}} - \mathrm{eU}$$

In this work, $\Delta G_{1\text{-}4}$ was calculated at U = 0.

3. Results and discussion

We synthesize $FeCoB_2$ powders by a simple borothermal reduction of metal oxides under Ar atmosphere with the assistance of

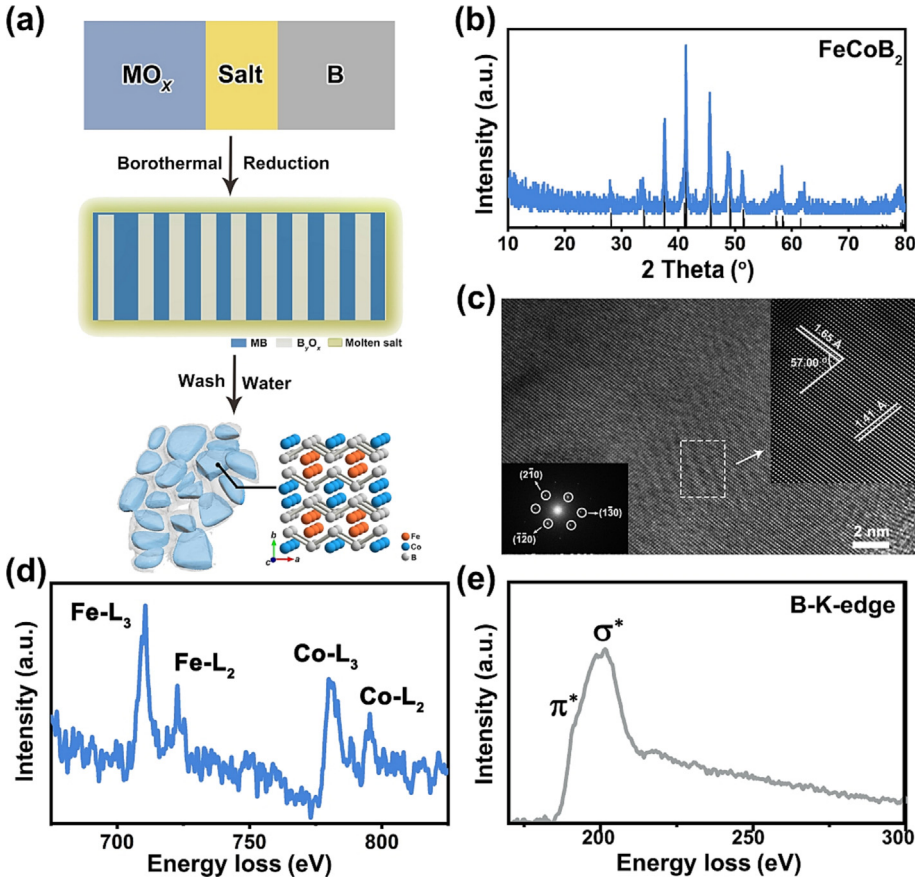

Fig. 1. (a) A schematic showing the synthesis and the crystal structure of $FeCoB_2$. (b) XRD pattern. (c) High-resolution transmission electron microscopy image (HRTEM) with inset of corresponding fast Fourier transform (FFT) image and IFFT image. (d) EELS of Co and Fe $L_{3,2}$ edges, respectively, (e) B K-edges of $FeCoB_2$.

NaCl-KCl (see Experimental Section for details). The schematic diagram of the synthesis process is shown in Fig. 1(a). Most metal oxides have a relatively high melting point. In molten salt, metal precursors are melted into monomers, which affords higher reactivity and higher reaction rates [38]. $FeCoB_2$ has an orthorhombic structure with a *Pnma* space group. The X-ray diffraction (XRD) patterns (Fig. 1b) indicate that our synthesized $FeCoB_2$ was phase-pure and highly crystalline (PDF# 612940). Transmission electron microscopy (TEM) images reveal that the $FeCoB_2$ surface is wrapped by nanosheets (Fig. S1a and b). It can be seen from the TEM image that the nanosheets are $FeCoB_2$ with low crystallinity (Fig. S1b). The inverse fast Fourier transform (IFFT) pattern is inserted in Fig. 1(c), and we can observe lattice fringes with interplanar spacings of 1.65 and 1.41 Å, corresponding to the $(\bar{1}\,\bar{2}0)$ and $(2\bar{1}0)$ planes of $FeCoB_2$, respectively. The acute angle between the two crystallographic planes is 57°, which is consistent with the theoretical crystallographic data of $FeCoB_2$. The results of energy dispersive X-ray spectroscopy (EDS) elemental mapping (Fig. S2) showed the uniform distribution of Fe, Co, and B elements. Electron energy loss spectroscopy (EELS) spectra were extracted from the edge of the sample in scanning transmission electron microscopy (STEM) mode (Figs. 1d and e and Fig. S3). EELS shows the pronounced Co and Fe $L_{3,2}$ edges at ~790 and 710 eV, respectively [39,40]. B K-edge is ~188 eV [41]. These EELS measurements further demonstrated the presence of the three elements.

Linear sweep voltammetry (LSV) polarization curves of $FeCoB_2$ were recorded (Fig. 2a), and the electrocatalyst was found to exhibit continuous activation over 10 cycles. During activation, its current density increased from 13 to 90 mA/cm^2 at 400 mV *vs* RHE. Subsequent cycles of $FeCoB_2$ lead to the same LSV curves as the 10th cycle, indicating that the $FeCoB_2$ forms a stable surface state (steady-state $FeCoB_2$ after OER is represented as the activated $FeCoB_2$). The activated $FeCoB_2$ showed ~7 times higher activity compared to the initial one. To further clarify this activation process, we first calculate the Pourbaix diagram of $FeCoB_2$ to evaluate the thermodynamically stable structure in the high pH region. As shown in Fig. 2(b), we observed that the most thermodynamically stable species in the working environment (U = 1–2 V *vs* RHE, pH 12–15) were CoOOH and $FeBO_3$ or their combinations. This result indicates that a phase transition readily occurs under OER conditions, and the metallic host tends to form the oxyhydroxides, while the boron is oxidized to the corresponding metal borate.

To experimentally demonstrate this concept, we performed a series of studies on $FeCoB_2$ after OER. The TEM images for the $FeCoB_2$ after the OER in Fig. S4 show the presence of an amorphous oxide layer with a thickness of 5–15 mm on the particle surface. Then, we investigated the chemical state of $FeCoB_2$ before and after the OER by using X-ray photoelectron spectroscopy (XPS), with all peaks calibrated with C 1s. The XPS peaks of Fe 2*p* and Co 2*p* shifted to higher binding energies after the OER compared to those before the catalytic reaction (Fig. S5). This result indicates that the oxidation state of the metal in the $FeCoB_2$ surface oxide layer is slightly elevated after the OER [30,42,43]. We further investigated the existence form of B in the oxide layer. For comparison, we also measured $FeCoBO_4$ with the same B-O structural unit as $FeBO_3$ and other forms of borates (Figs. S6 and S7a). The two peaks of B 1*s* in the $FeCoB_2$ before OER were assigned to the B-O and B^0/B-M

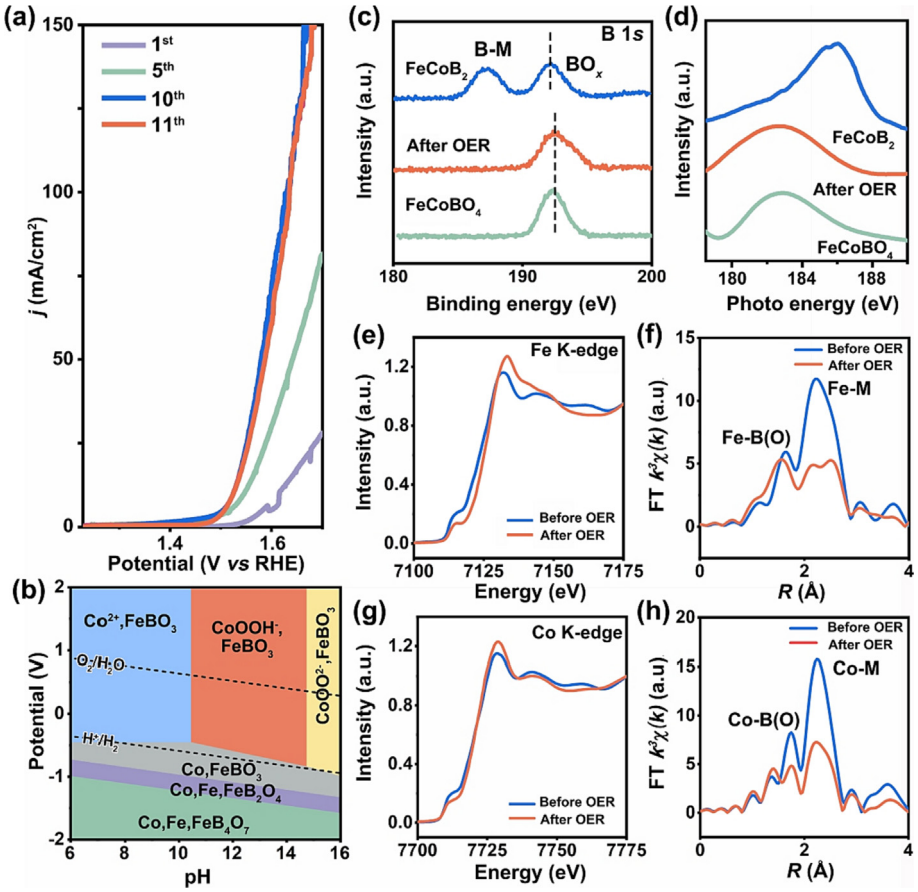

Fig. 2. (a) LSV polarization curves upon repetitive cycling for $FeCoB_2$. (b) Pourbaix diagram of $FeCoB_2$. (c) B 1*s* XPS and (d) B SXES spectrum of $FeCoB_2$ before and after the OER and $FeCoBO_4$. (e) XANES spectra and (f) EXAFS spectra at the Fe L-edge of $FeCoB_2$ before and after the OER. (g) XANES spectra and (h) EXAFS spectra at the Co L-edge of $FeCoB_2$ before and after the OER.

species, respectively (Fig. 2c). These results indicate that the surface of the $FeCoB_2$ before the OER has already been slightly oxidized when exposed to the air. The B 1*s* spectrum of $FeCoB_2$ after the OER shows a peak at 192.4 eV, which only has the same peak position as $FeCoBO_4$ [27,28]. We also performed the Soft X-ray emission spectrum (SXES) tests, and the B atom also exhibited the same peak position as $FeCoBO_4$ (Fig. 2d and Fig. S7b) [44]. The comparison of B1*s* XPS and SXES of $FeCoB_2$ before and after the OER revealed that the surface of $FeCoB_2$ was further oxidized during OER because the XPS peak of B in $FeCoB_2$ disappeared. The result also indicates that after the OER reaction, the stable boron species on the surface of $FeCoB_2$ is the borate and the B atoms existed in the same form as $FeBO_3$.

We further carried out X-ray absorption spectroscopy (XAS) tests to observe the local electronic structure changes of metal sites after OER. The Fe and Co K-edge X-ray absorption near-edge structures (XANES, Fig. 2e and g) show that the samples after OER have different electronic structures, indicating a change in the phase and structure of the material surface. The Fe and Co K-edge XANES spectra exhibit a positive energy shift, indicating that the valence states of metal atoms increased after catalysis [45,46]. This is consistent with our XPS results. To further probe the origin of these changes, we obtained the Fourier transform (FT) of the extended X-ray absorption fine structure (EXAFS, Fig. 2f and h) spectra. The activated $FeCoB_2$ shows two FT features: (1) The low-distance peak at ~1.5 Å represents M−O and M−B backscattering events. Since the interference periods of the two waves are almost equal, the presence of boron in the first coordination sphere is insignificant. However, it can be distinguished by a broader and lower peak intensity [42]. (2) The peak at ~2.5 Å originates from the nearest neighboring transition metal (M−M). The fitting parameters are summarized in Fig. S8 and Tables S1 and S2. It is not difficult to find that the M−M bond of Fe atoms is significantly longer, which is attributed to the phase transformation of iron to form borate ($FeBO_3$) on the material surface during the catalytic reaction. The crystal structure of $FeBO_3$ is shown in Fig. S9, and its M−M bond length is larger than that in $FeCoB_2$ (Table S3). However, the M−M bond of Co atoms has almost no change, due to the formation of oxyhydroxide (CoOOH) by Co atoms on the surface of the material after OER. The crystal structure and bond lengths of CoOOH are shown in Fig. S10 and Table S3. In short, $FeCoB_2$ acts as a precursor and undergoes a phase transition on the surface at a high oxidation potential, resulting in the transformation of the metal to the corresponding oxyhydroxide and B in the form of borate. This is also consistent with the following theoretical calculation results.

The electrocatalytic activity for OER of activated $FeCoB_2$ is investigated in 1 M KOH solution. For comparison, several reference materials including FeB, CoB, and commercially available RuO_2 are also studied under the same conditions (see details about

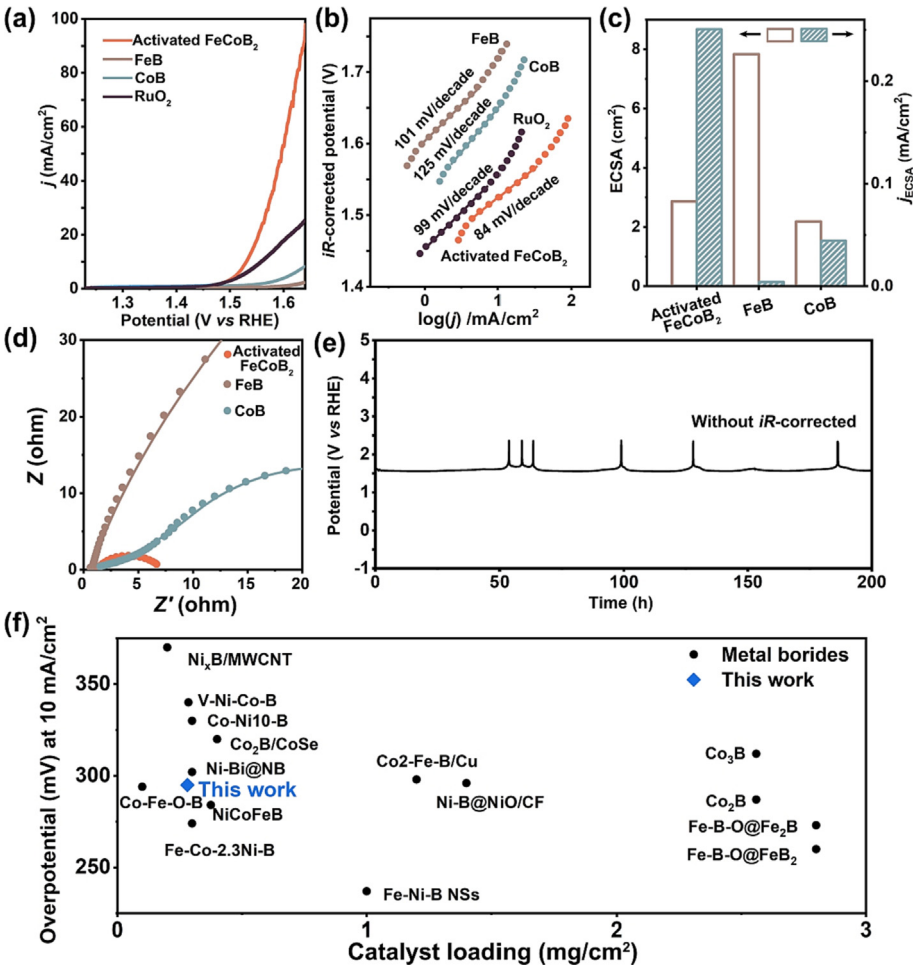

Fig. 3. (a) LSV curves toward OER of activated $FeCoB_2$, FeB, CoB, and RuO_2 in 0.5 M KOH electrolytes at a scan rate of 1 mV/s with 85% *iR*-compensations. (b) Tafel plots derived from (a). (c) Comparison of ECSA and specific activities (the currents were normalized by ECSAs) at 1.53 V_{RHE}. (d) Electrochemical impedance spectroscopy (EIS) Nyquist plots during OER of activated $FeCoB_2$, FeB and CoB. (e) Chronopotentiometry curve of activated $FeCoB_2$ at 10 mA/cm^2 current density. (f) Comparison of the electrocatalytic performance of activated $FeCoB_2$ with some non-noble metal boride OER catalysts [46–57].

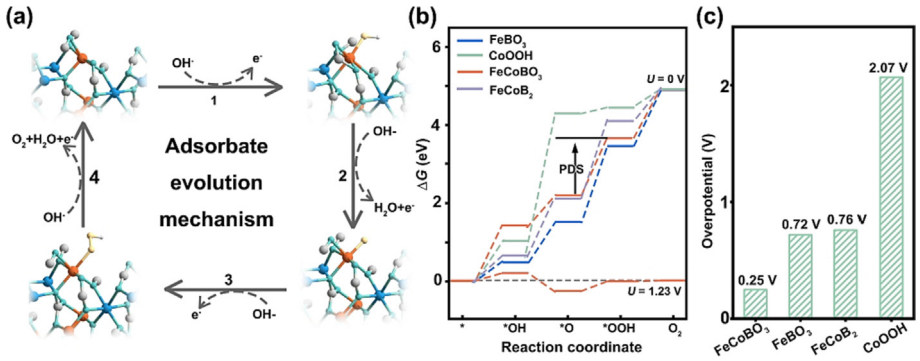

Fig. 4. (a) Schematic illustration of four-step reaction mechanism for OER. (b) Free energy diagram. (c) The comparison thermodynamic overpotential for $FeBO_3$, CoOOH, $FeCoB_2$ and $FeCoBO_3$ at 1.23 V vs RHE.

Electrochemical Measurements in the Experimental Section). Fig. 3 (a) shows the LSV curves towards OER with activated $FeCoB_2$, FeB, CoB, and RuO_2 as electrocatalysts. It is worth noting that activated $FeCoB_2$ exhibits excellent catalytic activity compared to FeB and CoB. Activated $FeCoB_2$ can achieve a current density of 10 mA/cm^2 at an overpotential of 295 mV, which is superior to the commercial RuO_2 (330 mV). More precisely, at 1.65 V, the current densities to activated $FeCoB_2$, FeB, CoB and RuO_2 reached 99, 3, 10 and 27 mA/cm^2, respectively. This means that the catalytic activity of activated $FeCoB_2$ is ~33, 10 and 3.7 times higher than that of FeB, CoB and RuO_2, respectively. Compared with the reported non-noble metal boride and other transition metal-based electrocatalysts, the activated $FeCoB_2$ still shows higher catalytic activity (Fig. 3f and Table S4). In addition, the Tafel slope of activated $FeCoB_2$ is ~84 mV/dec (Fig. 3b), which are smaller than that of RuO_2 (99 mV/dec), and much smaller than FeB (101 mV/dec) and CoB (125 mV/dec). This result demonstrates the faster OER catalytic kinetics of activated $FeCoB_2$. We further compared the intrinsic activity of activated $FeCoB_2$, FeB and CoB by normalizing the OER currents with respect to their electrochemical surface area (j_{ECSA}). As shown in Fig. 3(c), their intrinsic activity followed the same trend as the apparent activity. Fig. 3(d) shows the Nyquist plots for activated $FeCoB_2$, FeB and CoB. The values of series resistance (R_s) and charge transfer resistance (R_{ct}) for the three materials were extracted and summarized in Table S5 by fitting the experimental data to the corresponding equivalent circuit model (Fig. S14). It is not difficult to find that the R_{ct} and R_s values of activated $FeCoB_2$ is smaller than the other two materials. This result indicates that activated $FeCoB_2$ has faster reaction kinetics and better electrical transport properties. The chronopotentiometry (CP) was used to measure the stability of the activated $FeCoB_2$ catalysts (Fig. 3e), which was stable at a current density of 10 mA/cm^2 for 200 h. This result suggests that $FeCoB_2$ has outstanding catalytic stability. These results demonstrate that the activated $FeCoB_2$ leads to a significantly enhanced electrocatalytic activity for OER.

To exclusively clarify the effect of the in-situ formed surface structure on the catalytic activity, we performed density functional theory (DFT) calculations (see details about the Theoretical Section in Experimental Methods). We calculated the adsorption energies of various key intermediates (*OH, *O and *OOH) at the (100) face of the five models based on the $4e^-$ mechanism proposed by Nørskov et al. (Fig. 4a, Fig. S15) [58,59]. Fig. 4(b) shows a representative standard free energy diagram for all four-steps of OER at zero potential (U = 0 V) and equilibrium potential (U = 1.23 V). The largest reaction energies are considered potential-determining step (PDS) [54,60]. As shown in Fig. 4(b), the PDS of CoOOH is the deprotonation of *OH ($*OH + OH^* \rightarrow *O + H_2O + e^-$) and CoOOH (2.07 V) exhibits a higher reaction energy barrier at 1.23 V. The PDS of $FeCoB_2$, $FeBO_3$ and $FeCoBO_3$ is the *OOH formation step ($*O + OH^- \rightarrow *OOH + e^-$). In contrast, $FeCoBO_3$ (0.25 V) exhibited the lowest thermodynamic overpotential at 1.23 V (Fig. 4c and Table S6). Therefore, theoretical calculations clearly show that, the Fe site of $FeCoBO_3$ has the best OER activity among these five structures. These theoretical calculation results are consistent with our electrochemical testing. The results show that the metal borate-containing films formed on the $FeCoB_2$ surface are indeed the active sites. The guest non-metal elements affect the intrinsic activity of the metal sites and greatly reduce the energy barrier of the OER reaction, which enables the material to exhibit excellent catalytic activity.

4. Conclusions

In summary, we prepared $FeCoB_2$ and observed a phase transition on the surface during OER. Combining theoretical calculations and experimental characterizations, it demonstrates a proof-of-concept that the *in-situ* formed self-functional surface composed of metal borates is the catalytically active phase for the OER process. Such favorable microstructural features of metal borates enable to lower the OER energy barrier and thereof the materials to exhibit excellent catalytic activity (295 mV) and stability (200 h) in 1 M KOH. These findings provide new ideas for the rational design of electrocatalysts for various electrocatalytic reactions. For instance, with OER, instead of conducting that popular extrinsic treatment or modulation, full utilization of the intermediates offered from the undergoing OER as long-standing electrocatalysts will inspire the next generation of electrocatalysts design.

Declaration of competing interest

The authors declare that they have no known competing financial interests or personal relationships that could have appeared to influence the work reported in this paper.

Acknowledgments

Financially supported by the National Natural Science Foundation of China (51872115, 52101256, 51932003), China Postdoctoral Science Foundation Project (2020M680043), Science and Technology Research Project of the Department of Education of Jilin Province (JJKH20211083KJ), and 2020 International Cooperation Project of the Department of Science and Technology of Jilin Province (20200801001GH). The X-ray absorption spectra (XAS) of were collected at 4B9A diffraction experimental station in Beijing Synchrotron Radiation Facility (BSFR).

Appendix A. Supplementary data

Supplementary data to this article can be found online at https://doi.org/10.1016/j.jechem.2022.05.039.

References

[1] S. Chu, Y. Cui, N. Liu, Nat. Mater. 16 (2017) 16–22.
[2] T.R. Cook, D.K. Dogutan, S.Y. Reece, Y. Surendranath, T.S. Teets, D.G. Nocera, Chem. Rev. 110 (2010) 6474–6502.
[3] Z.W. She, J. Kibsgaard, C.F. Dickens, I. Chorkendorff, J.K. Nørskov, T.F. Jaramillo, Science 355 (2017) 4998.
[4] S. Chang, H. Zhang, Z. Zhang, J. Energy Chem. 56 (2021) 64–71.
[5] X. Zhang, X. Cheng, Q. Zhang, J. Energy Chem. 25 (2016) 967–984.
[6] X.-M. Liu, X. Cui, K. Dastafkan, H.-F. Wang, C. Tang, C. Zhao, A. Chen, C. He, M. Han, Q. Zhang, J. Energy Chem. 53 (2021) 290–302.
[7] S. Li, Z. Li, R. Ma, C. Gao, L. Liu, L. Hu, J. Zhu, T. Sun, Y. Tang, D. Liu, J. Wang, Angew. Chem. Int. Ed. 60 (2021) 3773–3780.
[8] H. Zhao, Z.-Y. Yuan, J. Energy Chem. 54 (2021) 89–104.
[9] Y. Zhu, Q. Lin, Z. Wang, D. Qi, Y. Yin, Y. Liu, X. Zhang, Z. Shao, H. Wang, J. Energy Chem. 52 (2021) 115–120.
[10] L. Tian, Z. Li, P. Wang, X. Zhai, X. Wang, T. Li, J. Energy Chem. 55 (2021) 279–294.
[11] Z. Xiao, C. Xie, Y. Wang, R. Chen, S. Wang, J. Energy Chem. 53 (2021) 208–225.
[12] Z.-J. Wang, M.-X. Jin, L. Zhang, A.-J. Wang, J.-J. Feng, J. Energy Chem. 53 (2021) 260–267.
[13] Q. Wang, L. Shang, R. Shi, X. Zhang, Y. Zhao, G.I.N. Waterhouse, L.-Z. Wu, C.-H. Tung, T. Zhang, Adv. Energy Mater. 7 (2017) 1700467.
[14] J. Chen, Q. Long, K. Xiao, T. Ouyang, N. Li, S. Ye, Z.-Q. Liu, Science Bulletin 66 (2021) 1063–1072.
[15] T. Wang, P. Wang, W. Zang, X. Li, D. Chen, Z. Kou, S. Mu, J. Wang, Adv. Funct. Mater 32 (2022) 2107382.
[16] X. Ding, H. Huang, Q. Wan, X. Guan, Y. Fang, S. Lin, D. Chen, Z. Xie, J. Energy Chem. 62 (2021) 415–422.
[17] K. Fan, H. Zou, Y. Ding, N.V.R.A. Dharanipragada, L. Fan, A.K. Inge, L. Duan, B. Zhang, L. Sun, Small 18 (2022) 2107249.
[18] X. Lv, Z. Xiao, H. Wang, X. Wang, L. Shan, F. Wang, C. Wei, X. Tang, Y. Chen, J. Energy Chem. 54 (2021) 626–638.
[19] W. Huang, C. Peng, J. Tang, F. Diao, M. Nulati Yesibolati, H. Sun, C. Engelbrekt, J. Zhang, X. Xiao, K.S. Mølhave, J. Energy Chem. 65 (2022) 78–88.
[20] C. Sommer, A. Adamska-Venkatesh, K. Pawlak, J.A. Birrell, O. Rüdiger, E.J. Reijerse, W. Lubitz, J. Am. Chem. Soc. 139 (2017) 1440–1443.
[21] D. Schilter, J.M. Camara, M.T. Huynh, S. Hammes-Schiffer, T.B. Rauchfuss, Chem. Rev. 116 (2016) 8693–8749.
[22] H. Chen, X. Zou, Inorg. Chem. Front. 7 (2020) 2248–2264.
[23] H.-L. Guang, S.-L. Zhu, Y.-Q. Liang, S.-L. Wu, Z.-Y. Li, S.-Y. Luo, Z.-D. Cui, A. Inoue, Rare Met. 40 (2021) 1031–1039.
[24] J. Nagamatsu, N. Nakagawa, T. Muranaka, Y. Zenitani, J. Akimitsu, Nature 410 (2001) 63–64.
[25] R.B. Kaner, J.J. Gilman, S.H. Tolbert, Science 308 (2005) 1268–1269.
[26] F. Guo, Y. Wu, H. Chen, Y. Liu, L. Yang, X. Ai, X. Zou, Energy Environ. Sci. 12 (2019) 684–692.
[27] J. Li, H. Chen, Y. Liu, R. Gao, X. Zou, J. Mater. Chem. A 7 (2019) 5288–5294.
[28] X. Jia, Y. Zhao, G. Chen, L. Shang, R. Shi, X. Kang, G.I.N. Waterhouse, L.-Z. Wu, C.-H. Tung, T. Zhang, Adv. Energy Mater. 6 (2016) 1502585.
[29] L. Wang, J. Li, X. Zhao, W. Hao, X. Ma, S. Li, Y. Guo, Adv. Mater. Interfaces 6 (2019) 1801690.
[30] Y. Wen, Z. Wei, J. Liu, R. Li, P. Wang, B. Zhou, X. Zhang, J. Li, Z. Li, J. Energy Chem. 52 (2021) 412–420.
[31] T. Qin, W. Zhang, Y. Ma, W. Zhang, T. Dong, X. Chu, T. Li, Z. Wang, N. Yue, H. Liu, L. Zheng, X. Fan, X. Lang, Q. Jiang, W. Zheng, Energy Storage Mater. 45 (2022) 33–39.
[32] M.B. Stevens, L.J. Enman, A.S. Batchellor, M.R. Vise, A.E. Cosby, C.D.M. Trang, S. W. Boettcher, Chem. Mater. 29 (2017) 120–140.
[33] C.C.L. McCrory, S. Jung, I.M. Ferrer, S.M. Chatman, J.C. Peters, T.F. Jaramillo, J. Am. Chem. Soc. 137 (2015) 4347–4357.
[34] G. Kresse, J. Furthmüller, Phys. Rev. B 54 (1996) 11169.
[35] P.E. Blöchl, Phys. Rev. B 50 (1994) 17953–17979.
[36] J.P. Perdew, K. Burke, M. Ernzerhof, Phys. Rev. Lett. 77 (1996) 3865–3868.
[37] A.H. Larsen, J. Phys. Condens. Matter 29 (2017) 273002.
[38] H. Jin, Q. Gu, B. Chen, C. Tang, Y. Zheng, H. Zhang, M. Jaroniec, S.-Z. Qiao, Chem 6 (2020) 2382–2394.
[39] T. Dong, W. Yi, T. Deng, T. Qin, X. Chu, H. Yang, L. Zheng, S.J. Yoo, J. Kim, Z. Wang, Y. Wang, W. Zhang, W. Zheng, Energy Environ. Mater. (2021), https://doi.org/10.1002/eem2.12262.
[40] R. Córdoba, R. Fernández-Pacheco, A. Fernández-Pacheco, A. Gloter, C. Magén, O. Stéphan, M.R. Ibarra, J.M. De Teresa, Nanoscale Res. Lett. 6 (2011) 592.
[41] F. Langenhorst, V.L. Solozhenko, Phys. Chem. Chem. Phys. 4 (2002) 5183–5188.
[42] N. Wang, A. Xu, P. Ou, S.-F. Hung, A. Ozden, Y.-R. Lu, J. Abed, Z. Wang, Y. Yan, M.-J. Sun, Y. Xia, M. Han, J. Han, K. Yao, F.-Y. Wu, P.-H. Chen, A. Vomiero, A. Seifitokaldani, X. Sun, D. Sinton, Y. Liu, E.H. Sargent, H. Liang, Nat. Commun. 12 (2021) 6089.
[43] A. Agui, S. Shin, M. Fujisawa, Y. Tezuka, T. Ishii, O. Mishima, K. Era, E. Shigemasa, A. Yagishita, J. Electron. Spectrosc. Relat. Phenom. 79 (1996) 191194.
[44] T. Deng, W. Zhang, O. Arcelus, J.-G. Kim, J. Carrasco, S.J. Yoo, W. Zheng, J. Wang, H. Tian, H. Zhang, X. Cui, T. Rojo, Nat. Commun. 8 (2017) 15194.
[45] H. Ren, X. Sun, C. Du, J. Zhao, D. Liu, W. Fang, S. Kumar, R. Chua, S. Meng, P. Kidkhunthod, L. Song, S. Li, S. Madhavi, Q. Yan, ACS Nano 13 (2019) 12969–12979.
[46] J. Jiang, M. Wang, W. Yan, X. Liu, J. Liu, J. Yang, L. Sun, Nano Energy 38 (2017) 175–184.
[47] Y. Guo, Z. Yao, C. Shang, E. Wang, ACS Appl. Mater. Interfaces 9 (2017) 39312–39317.
[48] J.M.V. Nsanzimana, Y. Peng, Y.Y. Xu, L. Thia, C. Wang, B.Y. Xia, X. Wang, Adv. Energy Mater. 8 (2018) 1701475.
[49] Y. Li, B. Huang, Y. Sun, M. Luo, Y. Yang, Y. Qin, L. Wang, C. Li, F. Lv, W. Zhang, S. Guo, Small 15 (2019) 1804212.
[50] W.-J. Jiang, S. Niu, T. Tang, Q.-H. Zhang, X.-Z. Liu, Y. Zhang, Y.-Y. Chen, J.-H. Li, L. Gu, L.-J. Wan, J.-S. Hu, Angew. Chem. Int. Ed. 56 (2017) 6572–6577.
[51] X. Ma, J. Wen, S. Zhang, H. Yuan, K. Li, F. Yan, X. Zhang, Y. Chen, ACS Sustainable Chem. Eng. 5 (2017) 10266–10274.
[52] H. Chen, S. Ouyang, M. Zhao, Y. Li, J. Ye, ACS Appl. Mater. Interfaces 9 (2017) 40333–40343.
[53] X. Chen, Z. Yu, L. Wei, Z. Zhou, S. Zhai, J. Chen, Y. Wang, Q. Huang, H.E. Karahan, X. Liao, Y. Chen, J. Mater. Chem. A 7 (2019) 764–774.
[54] H. Han, Y. Hong, J. Woo, S. Mhin, K.M. Kim, J. Kwon, H. Choi, Y. Chung, T. Song, Adv. Energy Mater. 9 (2019) 1803799.
[55] S. Gupta, M. Forster, A. Yadav, A.J. Cowan, N. Patel, M. Patel, ACS Appl. Energy Mater. 3 (2020) 7619–7628.
[56] J. Zhang, X. Li, Y. Liu, Z. Zeng, X. Cheng, Y. Wang, W. Tu, M. Pan, Nanoscale 10 (2018) (2002) 11997–111991.
[57] J.M.V. Nsanzimana, V. Reddu, Y. Peng, Z. Huang, C. Wang, X. Wang, Chem. Eur. J. 24 (2018) 18502–18511.
[58] M. Bajdich, M. García-Mota, A. Vojvodic, J.K. Nørskov, A.T. Bell, J. Am. Chem. Soc. 135 (2013) 13521–13530.
[59] J. Rossmeisl, A. Logadottir, J.K. Nørskov, Chem. Phys. 319 (2005) 178–184.
[60] M.T.M. Koper, J. Solid State Electrochem. 17 (2013) 339–344.